



www.adeepakpublishing.com

Knuuttila, O. et al. (2022): JoSS, Vol. 11, No. 3, pp. 1165–1186
(Peer-reviewed article available at www.jossonline.com)



www.JoSSonline.com

In-Space Radiometric Calibration of Nanosatellite Camera

Olli Knuuttila and Esa Kallio

Aalto University School of Electrical Engineering, Finland

Noora Partamies and Mikko Syrjäsoo

The University Centre, Svalbard, Norway

Olli Knuuttila, Kirsti Kauristie, Viktoria Sofieva, Ari-Matti Harri, Antti
Kestilä, Jarmo Kivekäs, Petri Koskimaa, Jouni Rynö, and
Johanna Tamminen

Finnish Meteorological Institute, Finland

Petri Kärhä

Aalto University School of Electrical Engineering, Finland

Juha-Matti Lukkari

Huld Oy, Finland

Arno Alho

Iceye Oy, Finland

Tuija Pulkkinen

University of Michigan, MI US

Abstract

Spacecraft payloads commonly include camera instruments; small satellites in particular provide new platforms for camera instruments. However, there remain challenges to the effective use of the images they produce in scientific and technological applications. This work presents a case study where images taken by the 1-unit (10 cm x 10 cm x 10 cm) Suomi 100 nanosatellite have been analyzed. Methods are introduced to overcome camera calibration difficulties, especially those caused by limited on-ground calibration and practical operational limitations. The methods developed in this study provide continuous space-based camera calibration during the lifetime of the satellite mission, forming the basis for the reliable usage of camera images. As an example of the approach developed, it is demonstrated how the camera calibration and image-processing methods can be used to maximize the scientific return of a small satellite's image of aurorae.

Corresponding Author: Olli Knuuttila – Email: olli.knuuttila@aalto.fi

Publication History: Submitted – 07/03/21; Revision Accepted – 04/27/22; Published – 10/06/22

1. Introduction

Low-cost small satellites known as nanosatellites (1–10 kg) provide new possibilities for space-based instrumentation, such as camera instruments. However, the small size of these satellites limits the volume, mass, and power consumption of the camera instrument. Small satellites also tend to have challenges with attitude control, which causes pointing problems and decreases the length of the available exposure times. Moreover, the nanosatellite can have such a small telemetry rate that the size of the downloaded images must be reduced either by reducing the number of pixels or by using data-compression algorithms. It is possible these days for research institutions with limited budgets to deploy such low-cost satellites and cameras, but severe budget and time constraints can result in less-than-ideal calibration of instruments before launch.

The present study describes efforts and methods developed to optimize the science return from a camera instrument on the Suomi 100 CubeSat (see Figure 1), which was launched on December 3, 2018. The satellite conforms to the 1-unit CubeSat standard, its size being 10 cm x 10 cm x 10 cm, and its mass being 1.3 kg. It has two science payloads, a wide-angle visible-light RGB camera and a radiospectrometer. The scientific goal of the satellite is to conduct space weather and geospace research by investigating aurorae and the properties of the ionosphere. The satellite's camera

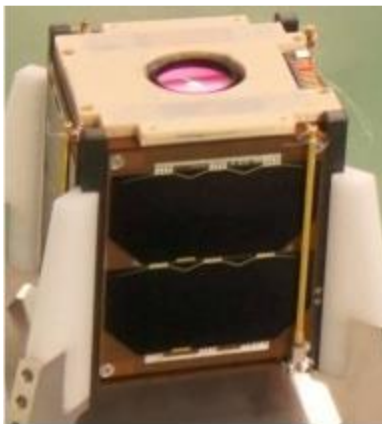


Figure 1: Suomi 100 satellite on September 12, 2018, just before it was installed into the launch adapter. The camera lens appears at the top of the satellite in the center of the light area. Photo credit: Jari Mäkinen.

was set up to capture aurorae, while the radiospectrometer was designed to investigate the propagation of the electromagnetic waves in the ionosphere.

The analysis in this work examines the case where the typical limitations and challenges of small satellites are mitigated by calibrating the camera instrument based on images of natural celestial objects (the Moon and stars) taken during flight. The study exemplifies how the analysis of images is complicated especially by the limited calibration done on ground, data compression, and the rotation of the spacecraft, i.e., by the typical issues that hamper the operation of small satellites.

The article is organized as follows: Section 2 describes the camera calibration method and how the laboratory measurements are used together with an image of stars and an image of the Moon. Models for the corresponding stars' light are then constructed and a model of lunar light is introduced. In Section 3, the derived calibration values are used to estimate the emission intensity of the aurorae captured in a night-time image taken by the satellite's camera. Finally, Section 4 discusses the potential of the developed tools and methods to maximize the performance of camera instruments onboard small satellites.

2. Camera Calibration Method

Figure 2 depicts an overview of the calibration steps described later in this Section. The process compares images taken both in the laboratory and in space, with the simulated values obtained from the models in order to derive the camera's quantum efficiency functions $h_k(\lambda)$ for different wavelengths λ for the three channels $k \in \{R, G, B\}$, where R , G , and B stand for red, green, and blue channels, respectively. The shape of $h_k(\lambda)$ is modeled by a set of free parameters, whose values are determined during calibration by optimizing the Huber loss between the observed channel values from the image and the modeled channel values. After calibration, the channel values from the aurora are compared to the modeled channel values. After calibration, the channel values from the aurora

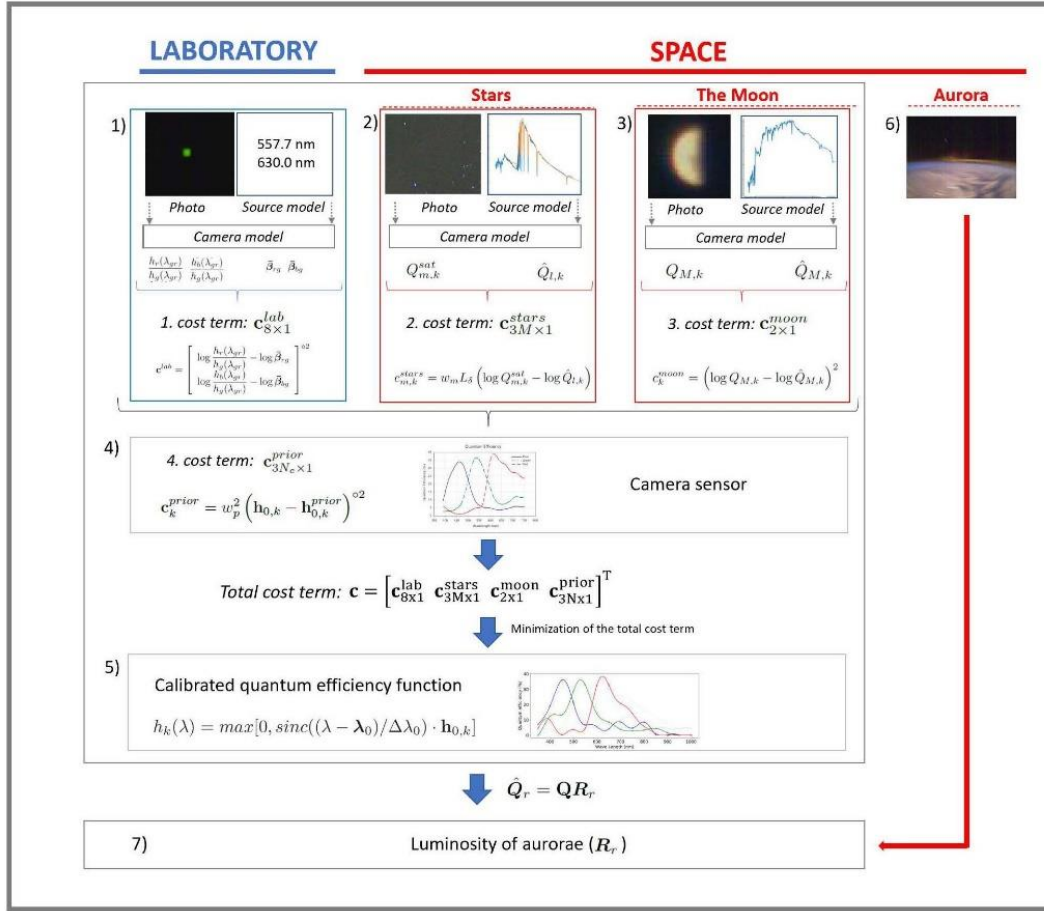


Figure 2. Illustration of the process where images taken by the Suomi 100 nanosatellite (1) in the laboratory and in space of (2) stars and (3) the Moon, are combined with (4) a priori camera sensitivity information to obtain (5) calibrated quantum efficiency functions $h_k(\lambda)$. Finally, the calibrated quantum efficiency functions are used to derive from (6) the image of an aurora (7) the luminosity of the aurora.

image are used to estimate the radiance R of the aurora at different emission line wavelengths.

Technically speaking, calibration is done developing the camera model (see Section 2.1), which is used to develop cost terms for the images taken in the laboratory $\mathbf{c}_{8 \times 1}^{lab}$ (see Section 2.2) and during flight depicting stars $\mathbf{c}_{3M \times 1}^{stars}$ (see Section 2.3) and the Moon $\mathbf{c}_{2 \times 1}^{moon}$ (see Section 2.4). The cost terms describe the difference between the observed channel values and the channel values obtained from the developed models of the lights from a monochromator in the laboratory, as well as models of the Moon light and star light. Finally, by adding the cost term associated with the a priori quantum efficiency functions $\mathbf{c}_{3N \times 1}^{prior}$ (see Section 2.5), the total cost function $\mathbf{c} = [\mathbf{c}_{8 \times 1}^{lab} \ \mathbf{c}_{3M \times 1}^{stars} \ \mathbf{c}_{2 \times 1}^{moon} \ \mathbf{c}_{3N \times 1}^{prior}]^T$ (see Section 2.5) can be

minimized to obtain the parameter values of the calibrated quantum efficiency functions of each channel (see Section 2.6), which gives the possibility to estimate the radiation of the imaged aurora (see Section 3).

2.1. Camera model

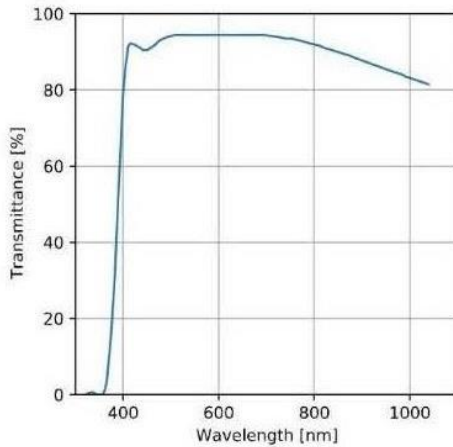
The camera on the Suomi 100 satellite is a GomSpace NanoCam with an Aptina CMOS RGB image sensor (MT9T031) and a Schneider-Kreuznach Cinegon 1.4/8 lens. For subsequent image analysis, the camera is modeled using the parameters from Table 1. Focal length together with sensor size can be used to calculate the horizontal and vertical fields of view, which are $FOV_x = 43.6^\circ$ and $FOV_y = 33.4^\circ$, respectively. SNR_{MAX} given in the sensor datasheet (Aptina

Table 1: Suomi 100 Satellite's Camera Parameters

Lens	Focal length	8.2 mm
	F-number	1.4
	Aperture area A	26.9 mm ²
	Transmittance function	Figure 3a
Sensor	Resolution	2048x1536
	ADC resolution	10-bit
	Pixel size	3.2x3.2 μm
	SNR_{MAX}	43 dB
	Quantum efficiency function	Figure 3 b

Imaging Corporation, 2006) can be used to calculate pixel-well capacity W ($= 10^{SNR_{MAX}/10} \approx 20,000 e^- = 20,000$ electrons), which is needed for mapping the electron counts to digital numbers.

The lens transmittance (Jos. Schneider Optische Werke GmbH, 2008) and the sensor quantum efficiency functions (Aptina Imaging Corporation, 2006) provided by the manufacturers are shown in Figure 3a–3b. These values give prior information which, as described in detail in Section 2.5, is used to derive the calibrated quantum efficiency functions. It should be noted that the present study focuses on the photometric calibration of the camera. In general, the analysis takes into account different geometric distortions, but does not try to model them.



The full photometric camera model takes spectral radiance $L(\lambda)[W/m^2/nm/sr]$ values incident on a pixel and produces the resulting RGB (Red-Green-Blue) values. The model is split into three parts: (i) the first part translates spectral radiance to spectral irradiance $F(\lambda)[W/m^2/nm]$ by estimating the varying pixel solid angles $\Omega_{i,j}$, where i and j are the pixel indices; (ii) the second part relates spectral irradiance with raw sensor activation values (referred to as digital numbers (DNs)); and (iii) the third part models the impact from image processing that was done by NanoCam.

Spectral irradiance is given by:

$$F_{i,j}(\lambda) = \Omega_{i,j}L(\lambda), \quad (1)$$

where the pixel solid angles $\Omega_{i,j}$ are calculated by assuming a pinhole camera model, projecting the corners of a sensor pixel (i,j) to the unit sphere, and then using the formula from (Mazonka, 2012):

$$\Omega = 2\pi - \sum_{k=1}^4 \arg \left[\frac{(s_{k-1} \cdot s_k)(s_k \cdot s_{k+1}) - (s_{k-1} \cdot s_{k+1})}{+i(s_{k-1} \cdot (s_k \times s_{k+1}))} \right], \quad (2)$$

where s_1, s_2, s_3 , and s_4 are unit vectors defined by the corners of the sensor pixel (i,j) . The pixel indices for

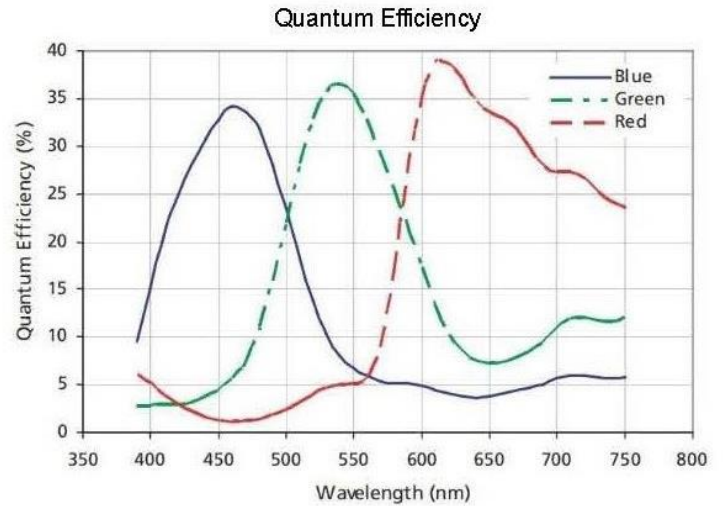


Figure 3: Lens transmittance (shown on left, Figure 3a) and image sensor quantum efficiency functions (right Figure, 3b) as given in their respective datasheets. The lens transmittance graph is reproduced from the datasheet.

Ω and the corner vectors were omitted for better readability. The formula requires circular indexing so that $k=0$ is $k=4$ and $k=5$ is $k=1$.

The first step in converting spectral irradiance $F_{i,j}(\lambda)$ into DNs, is to calculate the average photon count per wavelength, $N_{i,j}^y(\lambda)$, by:

$$N_{i,j}^y(\lambda) = E^y(\lambda)^{-1} T A F_{i,j}(\lambda), \quad (3)$$

where T is the image integration time, A is the aperture area as calculated from the focal length and F-number given in the lens datasheet, and $E^y(\lambda)$ is the photon energy calculated using the Planck-Einstein relation $E = hc/\lambda$. Shot noise, which is due to the Poisson-distributed random arrival of photons, can be ignored in our use case. The total predicted number of photons can then be obtained by integrating $N_{i,j}^y(\lambda)$ over all the wavelengths. In practice, when we integrate over the wavelengths, we do it over a limited wavelength range, which we selected to be $[\lambda_1 = 350 \text{ nm}, \lambda_2 = 1000 \text{ nm}]$, as we assume that the camera response is negligible outside this range. We can use $N_{i,j}^y(\lambda)$ to calculate $u_{i,j,k}(\lambda)$ [DN/nm], which represents how many DNs an impulse of photons of wavelength λ contribute to a pixel (i, j) belonging to the RGB channel k :

$$u_{i,j,k}(\lambda) = u_{max} G W^{-1} h_k(\lambda) N_{i,j}^y(\lambda) \quad (4)$$

Here, u_{max} is the maximum sensed value, G is the sensor gain, W [number of electrons] is the pixel well depth, and $h_k(\lambda)$ [number of electrons/photon] is the quantum efficiency function for the RGB channel k , which in our model also covers the transmittance function of the camera lens. Normally, u_{max} would be 1023 for 10-bit images ($2^{10}-1$). However, due to an undetermined reason, our images are consistently saturating at a lower DN count of 567, regardless of exposure or sensor gain settings. Therefore, we set $u_{max} = 567$ for our camera setup.

Finally, the model-predicted DN value $u_{i,j,k}$ is obtained when $u_{i,j,k}(\lambda)$ is integrated over the analyzed wavelength range $[\lambda_1, \lambda_2]$:

$$u_{i,j,k} = \int_{\lambda_1}^{\lambda_2} u_{i,j,k}(\lambda) d\lambda + T u_k^{dark} + u_k^{read}. \quad (5)$$

The term $T u_k^{dark}$ represents the predicted dark current-induced DNs due to the thermal noise of the sensor and it scales with the integration time T . We also include the predicted readout noise u_k^{read} in our model. We do not need to assume any specific distributions for these noise sources, as we only use their means. We will refer to these mean noise activation terms collectively as “background pixel activation.” During analysis, this background activation is always estimated and subtracted from the raw pixel readings to obtain the DN counts attributable to the various sources of interest. The estimated image-specific background activation will also cover any weak stray light possibly affecting the predominantly nighttime images. Figure 4(i) illustrates the aforementioned sensor modeling steps from the spectral radiance $h_k(\lambda)$.

Except for the quantum efficiency function, we will assume all other camera parameters to be known, and during calibration we will focus exclusively on estimating this function. We parameterized $h_k(\lambda)$ as a set of control points, which are then used together with Whittaker-Shannon interpolation (Whittaker, 1915) to produce a non-negative continuous function $h_k(\lambda)$:

$$h_k(\lambda) = \max[0, \text{sinc}((\lambda - \lambda_0)/\Delta\lambda_0) \cdot h_{0,k}], \quad (6)$$

where $\text{sinc}(x) = \sin(\pi x)/(\pi x)$, λ_0 is a vector with all the control point locations, and vector $h_{0,k}$ has the corresponding control point values. The control point locations are specified based on the camera model minimum and maximum wavelengths ($\lambda_{min}, \lambda_{max}$) and the total number of control points N_c so as to be separated by equal distances $\Delta\lambda_0 = (\lambda_{max} - \lambda_{min})/(N_c - 1)$. We considered various other interpolation methods and settled on the current one as it produced the lowest cost function scores during calibration.

A significant amount of image processing was done by NanoCam (see Figure 4(ii)). To establish a relation between downlinked images and the irradiance maps that produced them, we follow a two-step procedure, where we first estimate the original raw image by inverting this processing chain. After that, we use a camera model to link the resulting digital numbers (DN) of the raw image and the image exposure time to irradiance values. The lossy image-processing steps

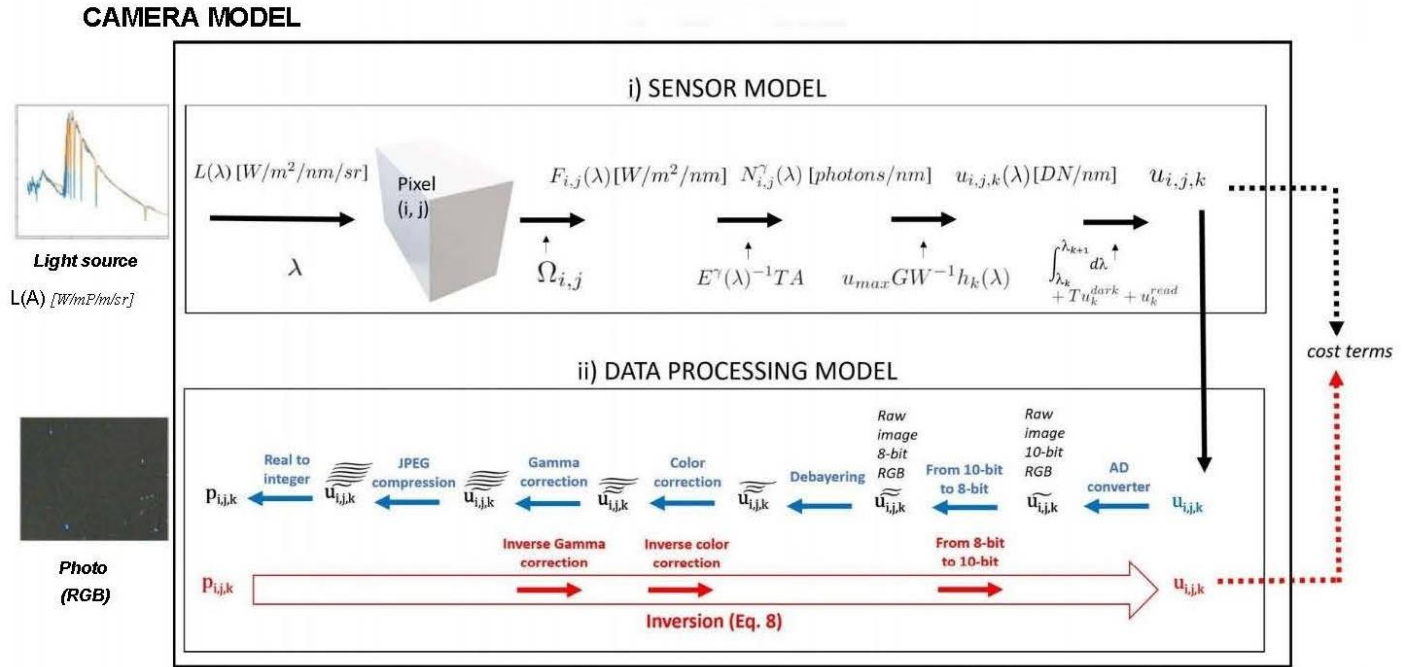


Figure 4. Schematic illustration of the developed camera model: (i) a flowchart of the sensor modeling steps from the spectral radiance $L(\lambda)$ to the expected raw sensor readings ($u_{i,j,k}$); (ii) An illustration of how the Suomi 100 camera instrument processes the raw image ($u_{i,j,k}$) to the final RGB values ($p_{i,j,k}$). Blue arrows pointing from left to right show the camera onboard processing steps. The text and lines presented in red color show which parts of the onboard processing are included in the inversion process where the RGB values in the image (red color $p_{i,j,k}$) are used to derive estimated initial DN's (red color ($u_{i,j,k}$)). Steps (i) and (ii) form the camera model that is used to derive the cost terms (dashed lines). See text for details.

lead to increased noise in the irradiance estimates, and to certain difficulties when trying to determine the camera model parameters.

As we do not attempt to model error variances and only use the mean expected DN's for calibration, we can disregard the steps that introduce a zero-mean error term to the DN's. We assume that the system debayering algorithm interpolates missing channel values based on nearby same-channel values, resulting only in zero-mean errors. The JPEG compression error is composed of rounding, quantization, and truncation errors, of which the latter has a non-zero mean if a given 8x8 compression block contains the values 0 or 255 (Luo et al., 2010). The impact from this truncation term is deemed negligible, as our images have a background level above zero and saturation is addressed directly by either excluding saturated measurements, or as is the case of moderately saturated stars, by mitigating the saturation effect by modeling it. In addition to

the processing chain inversion, the effect of warm pixels is removed by image-specific background subtraction methods, each one discussed later.

The parts of the processing chain that we will invert can be expressed as:

$$p_{i,j} = (2^8 - 1) \text{gamma}_{\gamma, b_p} \left(\frac{1}{2^{10} - 1} \mathbf{K}_{3 \times 3} u_{i,j} \right), \quad (7)$$

where $u_{i,j}$ is a column vector of pixel (i, j) raw RGB values, $p_{i,j}$ is the resulting image pixel, $\mathbf{K}_{3 \times 3}$ is a known color-correction matrix and $\text{gamma}_{\gamma, b_p}$ is the gamma-correction function with the main parameter $\gamma = 2.2$ and break point $b_p = 0.1$, which defines the linear region for low pixel values. The gamma-correction function is defined for pixel values scaled to the range 0–1. This is why we need to divide the 10-bit raw image pixel values by $2^{10} - 1$. Due to the bit depth reduction, we scale the values back based on 8-bits instead of 10-bits by multiplying with $2^8 - 1$. We chose to ignore that the operations were done on-board using integer math, as these effects cannot be inverted.

By solving for $\mathbf{u}_{i,j}$, we finally obtain the pixel-wise inversion:

$$\mathbf{u}_{i,j} = K^{-1}(2^{10} - 1) \text{invgamma}_{\gamma,b_p} \left(\frac{1}{2^8 - 1} p_{i,j} \right), \quad (8)$$

where the $\text{gamma}_{\gamma,b_p}(x)$ and $\text{invgamma}_{\gamma,b_p}(x)$ functions (MathWorks, 2006) are defined for $x \in [0,1]$ as:

$$\text{gamma}_{\gamma,b_p}(x) = \begin{cases} x s_{ls} & x \leq b_p \\ f_s x^{1/\gamma} - c_o & x > b_p \end{cases} \quad (9)$$

$$\text{invgamma}_{\gamma,b_p}(x) = \begin{cases} \frac{x}{s_{ls}} & x \leq s_{ls} b_p \\ \left(\frac{x + c_o}{f_s} \right)^\gamma & x > s_{ls} b_p \end{cases} \quad (10)$$

where

$$s_{ls} = (\gamma b_p^{1-1/\gamma} - \gamma b_p + b_p)^{-1} \quad (11)$$

$$f_s = \gamma s_{ls} b_p^{1-1/\gamma}$$

$$c_o = f_s b_p^{1/\gamma} - s_{ls} b_p$$

In the following sections, we will go through the different measurements that will be used to estimate the overall camera quantum efficiency function $h_k(\lambda)$.

2.2. Preflight measurements (\mathbf{c}^{lab})

A small calibration campaign was performed before launch of the Suomi 100 satellite, where images were taken of a diffuse surface illuminated in turn with monochromatic light at 557.7 nm (green) and at 630 nm (red) wavelengths corresponding to prominent auroral emission lines. The light source full width at half maximum (FWHM) was 1 nanometer. Images were taken with two exposure times, 50 ms and 150 ms. The targets were imaged both at the center and at the side of the images. For each test setup, five dark images were taken before a batch of ten actual measurements. During these measurements, the satellite was inside a 3 mm acrylic sheet container, leading to an approximate 8–10% loss in transmittance. The transmittance function of acrylic plastic is expected to be very flat in the 450–800 nm range. Default camera settings were

used so that the resulting images were JPEG compressed, i.e., they went through the full image-processing chain. With hindsight, it would have been more useful to capture the raw images instead. The JPEG compression at 85% quality setting affects the pixel variance of the illuminated surface in an intractable manner, so that shot noise, and thus full well capacity, is impossible to estimate using the calibration images. The monochromatic 630 nm light produces a strong response from the sensor R-band, but only a weak response from the Band G-bands. The color-correction coefficients lead to negative B- and G-band values, which are then clamped to zero, leading to a loss of information preventing correct inversion of the color-correction step for these areas of the images. The same occurs with 557.7 nm, but only for the B-band, so that the G- and R-bands are unaffected.

Gamma correction is inverted for both actual and dark images. A mean dark image is subtracted from the actual images before calculating the mean pixel values of the illuminated target in order to remove the effects of dark current and readout noise. This results in negative values on the problem bands as the background activation creates a buffer preventing the clamping from happening immediately. If no clamping occurs, color correction is still a linear operation.

Based on the measurements (see Table 2), it would seem that the sensor response is not strictly linear with respect to the measured radiance as the ratio of mean pixel values between 150 ms and 50 ms exposures is consistently lower than 300%. A more comprehensive calibration campaign would be needed to determine the source of this non-linearity and, if necessary, to produce a model for it.

We can gain some information about the quantum efficiency curve by comparing the mean pixel values after also inverting the color-correction step for the 557.7 nm images (see Table 3). This can be done by inverting the color-correction matrix. Both actual and dark images were inverse color-corrected before background subtraction.

Table 2. Color-Corrected Mean Pixel Values of the Target Surface, as Measured at the Laboratory

A [nm]	Exp [ms]	Center target			Side target		
		R	G	B	R	G	B
557.7	50	9.6	46.8	-2.9	6.5	33.4	-2.5
	150	25.6	133.9	-7.5	17.9	95.8	-7.0
	150/50	267%	286%	259%	275%	287%	280%
630.0	50	38.9	-6.5	-5.9	27.9	-5.3	-4.1
	150	110.5	-8.0	-8.3	78.6	-8.3	-8.3
	150/50	284%	123%	141%	282%	157%	202%

Table 3. Pixel Values after Color-Correction Inversion at 557.7 nm, as Measured at the Laboratory

	Center			Side			Center		Side	
Exp [ms]	R	G	B	R	G	B	R/G	B/G	R/G	B/G
50	5.69	21.87	5.13	3.74	15.41	3.34	26.00	23.44	24.24	21.64
	±0.006	±0.009	±0.006	±0.005	±0.007	±0.005	±0.03%	±0.03%	±0.03%	±0.03%
150	15.50	62.69	15.04	10.46	44.34	9.69	24.72	24.00	23.58	21.85
	±0.009	±0.023	±0.008	±0.007	±0.016	±0.006	±0.02%	±0.02%	±0.02%	±0.02%
150/50	272.5	286.6	293.4	279.9	287.7	290.5				
	±0.3%	±0.2%	±0.4%	±0.4%	±0.2%	±0.5%				

The mean RGB pixel values and the standard error of the mean for different target locations at different exposure times. Calculated ratios are shown with a gray background. The standard error of the ratios is estimated as a ratio of two normally distributed variables using an approximation (Diaz-Frances and Rubio, 2013).

Based on the sensor datasheet image (Figure 3b), the quantum efficiency at $\lambda_{gr} = 557.7$ nm for R, G and B channels would roughly be 6%, 33%, and 6%, respectively. This would predict the same ratio of 18% for both R/G and B/G values. The estimated B/G ratios β_{bg} (21–24%) might not be accurate because of the B-channel clamping after color correction, even though it seems to have survived intact because of the image background acting as a buffer. Also, the estimated R/G ratios (β_{rg} (24–26%)) are noticeably higher than indicated by the datasheet.

For calibration, the measured values of the two ratios, $\bar{\beta}_{rg} = [0.26, 0.25, 0.24, 0.24]^T$ and $\bar{\beta}_{bg} = [0.23, 0.24, 0.21, 0.22]^T$, contribute the following cost term, c^{lab} , for the least-squares optimization method:

$$c^{lab} = \left[\begin{array}{cc} \log \frac{h_r(\lambda_{gr})}{h_g(\lambda_{gr})} & -\log \bar{\beta}_{rg} \\ \log \frac{h_b(\lambda_{gr})}{h_g(\lambda_{gr})} & -\log \bar{\beta}_{bg} \end{array} \right]^{\circ 2}, \quad (12)$$

where $(\cdot)^{\circ(\cdot)}$ is the element-wise power operator. The logarithm of the ratios is used as it is also used for the

star and the Moon measurements. It gives a common scale to these different measurement types.

2.3. Stars (c^{stars})

In January 2019, we captured an image sequence of the Orion constellation. Eight small images, so-called “thumbnails” of size 128×96 pixels were downlinked (Figure 5). Based on them, one full resolution image was chosen to be downlinked. The image (see Figure 6) shows prominent stars such as Procyon, Sirius, Betelgeuse, and Rigel. Also worth mentioning is the Orion nebula below the belt of Orion. There is a radiation-induced feature going almost perpendicular to the general motion of the stars. Its edges are very sharp, which is also a telltale sign that the feature was not caused by visible light coming through the lens. Even though lens point spread function and motion blur spreads out the starlight, many of the stars have over-exposed pixels due to the high gain settings used onboard the satellite.

After estimating the raw image by inverting the image processing using Eq. (8), we remove the vertical

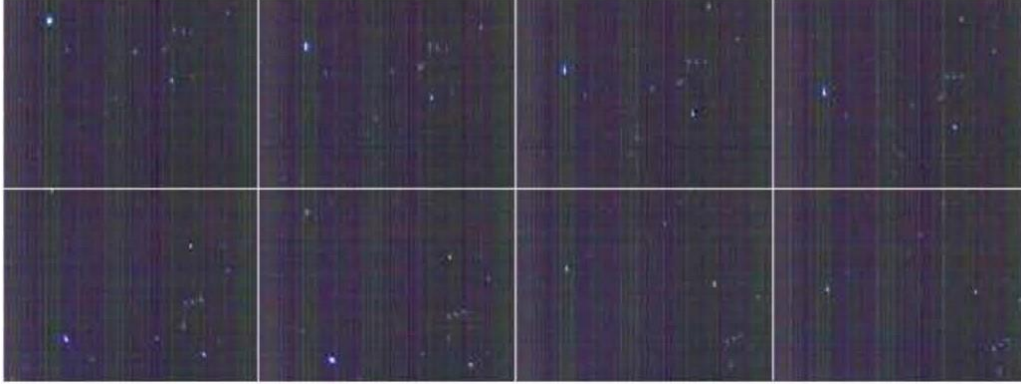


Figure 5: Eight thumbnails of consecutively taken images on 2019-01-23 (#1259-1266) of the Orion constellation. The images were taken with $T = 1.6$ s exposure, an analog gain of x8, and a digital gain of x4 (for a total sensor gain $G = 32$). An additional x4 gain was given for this illustration.

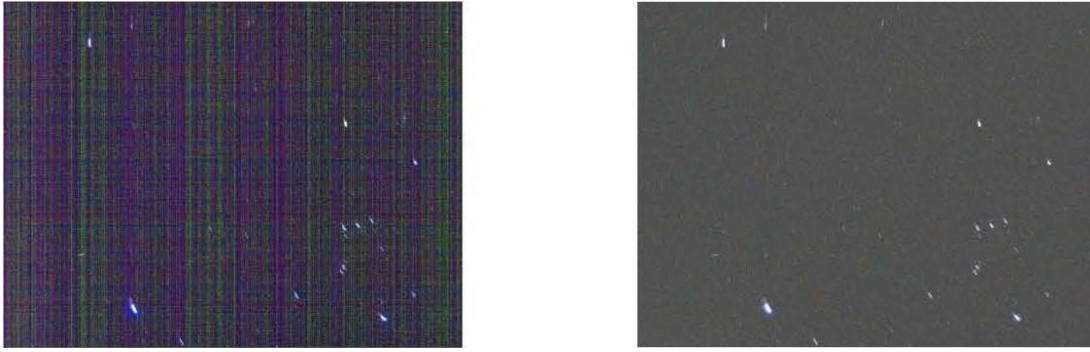


Figure 6: Image #1264 of the Orion constellation. Left: On-board processed image with extra x4 gain. Right: The estimated raw image after stripe removal with extra x4 gain.

and horizontal stripes by subtracting first the column-wise median, and then the row-wise median values from the image. The processed image can be seen in Figure 6b. The stars are detected using the DAOFIND algorithm (Stetson, 1987) (see Figure 7). The DNs induced by each star are estimated by summing the pixel values inside a circular mask centered on the brightness centroid of each star. The size of the mask is varied heuristically based on the detection strength so that a larger mask is used for brighter stars. The remaining background noise contribution is estimated by taking the median of each channel over the whole image. The empirical starlight DN count $\hat{Q}_{i,k}^{star}$ channel k for star l is calculated by:

$$\hat{Q}_{i,k}^{star} = \sum_{i,j \in M_l} u_{i,j,k} - \text{median}_{i,j}(u_{i,j,k}) \sum_{i,j \in M_l} 1 \quad (13)$$

where $u_{i,j,k}$ is the channel k value of pixel (i, j) and M_l is the mask for detected star l .

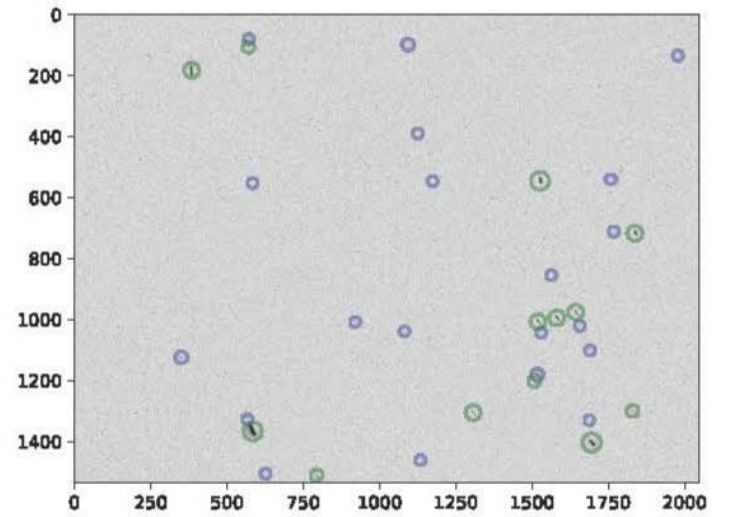


Figure 7: Inverted square-root image of the image #1264 shown in Figure 6b after stripe removal with DAOFIND detections. Green circles are detections that have been successfully matched to the Hipparcos catalog.

The detected stars are matched with the Hipparchos catalog (Perryman et al., 1997) based on their location and apparent magnitude. The catalog is queried based on an initial guess of the image- frame orientation, the camera field-of-view and a limiting apparent magnitude of 3.0. This value was empirically selected, to exclude stars with weak signal-to-noise ratios. The stars are projected to the image plane and each detected star l is assigned the closest projected star m . An empirical star magnitude \hat{V}_{mag}^l is calculated by summing the DN's of each channel and then subtracting the median difference between the preliminary initial empirical star magnitudes \hat{V}_{ini}^l and the matched actual star magnitudes V_{mag}^m as:

$$\hat{V}_{ini}^l = 2.5 \log_{10} \sum_{k \in \{r, g, b\}} \hat{Q}_{l,k}^{star}, \quad (14)$$

$$\hat{V}_{mag}^l = \hat{V}_{ini}^l - \text{median}(\hat{V}_{ini}^l - V_{mag}^m). \quad (15)$$

Matches with $abs(\hat{V}_{mag}^l - V_{mag}^m) > 2.0$ or with a distance in image space higher than 100 px are discarded, the initial orientation guess being refined using least-squares optimization based on the remaining matched stars. The matching process is redone iteratively until the initial orientation changes less than a certain threshold. After the final iteration, all matches with image space distance greater than 40 px are discarded.

To constrain our camera model parameters, and particularly the quantum efficiency curves of each channel, we need the source spectra $F_{m,\lambda}$ for the matched stars m . It proved to be very difficult to find low to medium resolution optical (~300–900 nm) spectra for bright stars with apparent magnitude less than 3. Because of this, we ended up with a hybrid approach, where we used star spectra measured by the GOMOS mission in wavelength ranges of 350–690 nm, 755–775 nm, and 926–954 nm (Bertaux et al., 2010; Tamminen et al., 2010), and for the gaps in the spectra (690–755 nm, 775–926 nm, and 954–1000 nm), we used the Castelli & Kurucz (2004) stellar atmosphere model. The model is implemented in Py-Synphot (Laidler et al., 2008), a Python module used

for processing Hubble Space Telescope data. For each star, the model needs effective temperature T_{eff} , log surface gravity $\log(g)$, and metallicity Fe/H . Effective temperature dominates the form of the spectrum, while surface gravity and especially metallicity affects it only slightly.

Initially, we manually searched the VizieR (Ochsenbein et al., 2000) and Simbad (Wenger et al., 2000) databases, and found that for a few stars the research converged quite well on a small range of relevant star parameters. However, there were many stars for which a wide range of different parameter values were suggested. Deciding case by case which study to believe was not an option, so we decided to use the median value extracted from the Pastel catalog (Soubiran et al., 2016), which is a collection of data from various studies. However, we could not find values for all the stars from there, and thus ended up searching from Wu et al. (2011), and that failing, from McDonald et al. (2017). The star parameters found are shown in Table 4, and both modeled and GOMOS-based spectra can be seen in Figure 8.

Table 4. Matched Stars from the Suomi 100 Satellite's Camera Image Shown in Figure 7, which was used in the Calibration

Name	Bayer	HIP	\hat{V}_{mag}	V_{mag}	T_{eff}	$\log(g)$	Fe/H
Sirius ^a	* alf CMa	32349	-0.41	-1.46	9847	4.3	0.49
Rigel ^a	* bet Ori	24436	0.53	0.13	9379	0.863	
Procyon	* alf CMi	37279	0.73	0.37	6586	4	-0.015
Betelgeuse	* alf Ori	27989	1.1	0.708	3540	0.00	0.05
Bellatrix	* gam Ori	25336	1.64	1.64	22339	3.84	-0.07
Alnilam	* eps Ori	26311	1.5	1.69	15339	1.574	
Alnitak	* zet Ori	26727	1.59	1.74	20788	2.409	
Mirzam	* bet CMa	30324	1.88	1.97	24953	3.624	
Saiph	* kap Ori	27366	1.93	2.06	15257	2.662	
Mintaka	* del Ori	25930	2.06	2.25	21298	3.21	
Hatysa ^b	* iot Ori	26241 26197 26199	2.06	2.77	33135	3.667	
Cursa	* bet Eri	23875	2.87	2.79	8002	3.78	-0.2
Gomeisa	* bet CMi	36188	2.9	2.89	8197	3.12	

^a Sirius and Rigel are excluded from calibration as they are very bright and saturated.

^b Hatysa is excluded from calibration as it is too close to the Orion nebula. The columns from left to right are the name of the star, it's Bayer designation, Hipparchos ID, initial apparent magnitude estimate, apparent magnitude given in literature, effective temperature in Kelvins, log surface gravity, and metallicity.

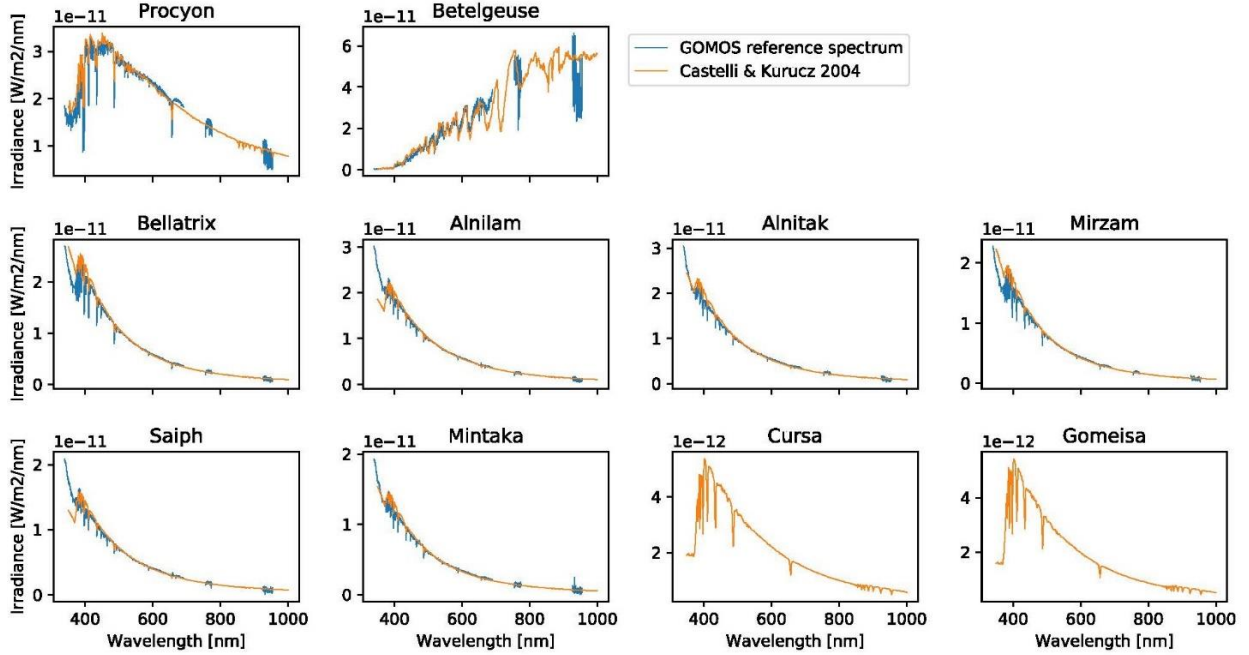


Figure 8. The spectra measured during the GOMOS mission is used preferentially. If it is missing, the stellar atmosphere model by Castelli and Kurucz, 2004, is used instead. The parameters needed by the model were searched from various sources (see text).

We made one exception with Betelgeuse, as the image was taken during an exceptionally strong dimming event of the variable star. We did not want to exclude the measurement as it is the only relatively cold star imaged and could thus provide valuable data to constrain the spectral response of our camera. We adjusted the apparent magnitude from 0.42 to 0.708, based on observations made by the CTOA observer on January 24, 2019 accessed through the AAVSO International Database (Kafka, 2020). The GOMOS spectrum for Betelgeuse was renormalized to this apparent magnitude. Additionally, so the modeled spectrum would better match the GOMOS spectrum, the effective temperature, surface gravity, and metallicity were obtained from (Ramirez et al., 2000) instead of the Pastel catalog.

To perform camera model calibration, we need to calculate the predicted total DN_s $Q_{m,k}^{star}$ that can be attributed to each star m in each RGB channel k given our model parameters. These DN_s can be spread out over various pixels. We do this by integrating over the camera model (Eqs. (3), (4), and (6)) and the synthetic source spectrum $F_m(\lambda)$ to obtain an ideal DN count $\tilde{Q}_{m,k}$, which does not take into account the saturation of pixels:

$$\tilde{Q}_{m,k} = u_{max} G W^{-1} T A \int_{\lambda_{min}}^{\lambda_{max}} h_k(\lambda) E^\gamma(\lambda)^{-1} F_m(\lambda) d\lambda, \quad (16)$$

where λ_{min} and λ_{max} specify the valid range of wavelengths of our camera model and other parameters, as in Eqs. (3) and (4).

Equation (16) would be enough if we were to ignore the four brightest stars with saturated pixels. However, in an attempt to use as many data points as possible, we developed the following method, where we model per-pixel saturation by assuming a Gaussian point spread function (PSF) and convolve it with the estimated motion blur path. The paths of the stars are modeled by line segments whose length and orientation are calculated based on an estimated image plane rotation center and the estimated angle that the image was rotated during exposure. The rotation center ($i_c = 2727, j_c = 262$) and the rotation angle ($\alpha = 0.71^\circ$) were determined manually by fitting lines to the motion trails left by the stars in the image. In practice, the convolution is done at discrete points between a PSF lattice $f^{psf}(\sigma)$ and a line segment lattice k_m^{blur} . The resulting lattice is normalized so that its elements $k_{m,\bar{i},\bar{j}}$ sum to one. We use \bar{i} and \bar{j} for the lattice indices so as to

distinguish the m from the image coordinate symbols i and j .

The unknown background noise level reduces the usable pixel value range as less starlight can be gathered before saturation. We estimate the effective saturation limit $\hat{u}_{max} = 525.6$ by selecting bright pixels in each channel using a threshold of DN 560 and then using morphological operations (dilation and erosion) to select those pixels belonging to the four brightest stars that are most likely affected by saturation. The effective saturation limit is then obtained by calculating the mean value of these pixels and subtracting the median pixel value calculated from the whole image. Based on this, if we assume negligible background noise for other, short exposure time bright images that saturate at DN 567, we can estimate the unknown background noise level to be around 41.4 for the star image.

Now, the predicted and possibly saturated, DN count ($Q_{m,k}^{star}$) induced by a star m can be expressed as:

$$\begin{aligned} \bar{k}_{m,\bar{l},\bar{j}} &= (f^{psf}(\sigma) * k_m^{blur})_{\bar{l},\bar{j}} \\ k_{m,\bar{l},\bar{j}} &= \bar{k}_{m,\bar{l},\bar{j}} \left(\sum_{\bar{l},\bar{j}} \bar{k}_{m,\bar{l},\bar{j}} \right)^{-1} \\ Q_{m,k}^{star} &= \sum_{\bar{l},\bar{j}} \min(\hat{u}_{max}, \tilde{Q}_{m,k}^{star} k_{m,\bar{l},\bar{j}}), \end{aligned} \quad (17)$$

where σ is the standard deviation of the circular symmetric PSF. The parameter σ defining the PSF needs

to be estimated during calibration. If no saturation occurs at any $k_{m,\bar{l},\bar{j}}$, the saturated DN count $Q_{m,k}^{star} = \tilde{Q}_{m,k}^{star}$. The predicted pixelwise DN responses ($Q_{m,k}^{star}$ before summing) of the six brightest stars together with the corresponding image regions are shown in Figure 9. We tried to model the lowering of the pixelwise DN counts due to saturating readout noise using the mean of a truncated normal distribution. However, we noticed that the noise can exceed the undetermined saturation point $u_{max} = 567$ and thus the actual noise mean is close to zero even at the most saturated image regions.

The empirical starlight DN counts $\hat{Q}_{l,k}^{star}$ from Eq. (13) contribute the following cost terms, $c_{m,k}^{stars}$, for the least squares method:

$$c_{m,k}^{stars} = w_m L_\delta(\log Q_{m,k}^{star} - \log \hat{Q}_{l,k}^{star}), (l, m) \in \mathcal{M} \\ k \in \{R, G, B\} \quad (18)$$

where $L_\delta(\cdot)$ is the Pseudo-Huber-loss function defined as:

$$L_\delta(a) = \delta^2 \left(\sqrt{1 + (\alpha/\delta)^2} - 1 \right). \quad (19)$$

The values of the \mathcal{M} is a set of tuples connecting the detected and successfully matched stars, and the w_m is a weight term calculated for each star m based on the effective temperatures $T_{m,eff}$ of all the matched stars. We use the logarithm of the star DN counts for the residual, so that bright stars with many saturated pixels will not dominate the optimization. The purpose of the

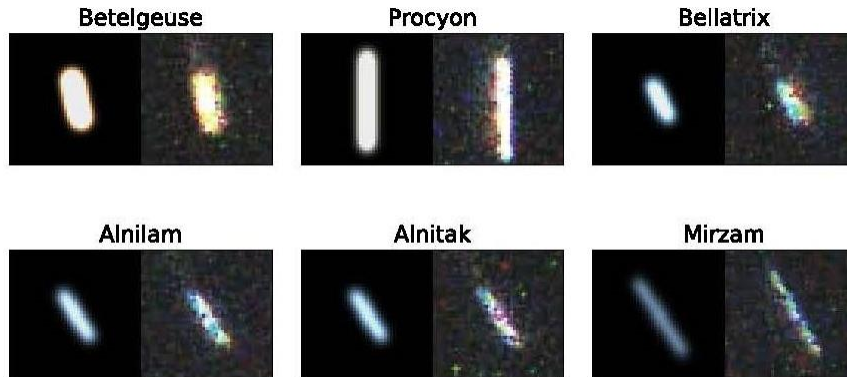


Figure 9: Predicted pixel wise DN responses (left) of the six brightest stars, together with the corresponding image regions (right). The lattices were calculated using calibrated model parameters.

weight term is to balance the optimization more evenly across different star temperatures by increasing the weight of stars with a rare temperature. The weight is calculated based on an inverted sample count, where the samples are discounted based on the peak wavelength difference, using a Gaussian kernel:

$$w_m = \left[\sum_{(i,n) \in \mathcal{M}} e^{-0.5\sigma_\lambda^{-2}[\lambda_p(T_{m,eff}) - \lambda_p(T_{n,eff})]^2} \right]^{-1} \quad (20)$$

where $\sigma_\lambda = 100$ nm is the length scale used and $\lambda_p(T_{eff})$ is the Wien's displacement law for the peak wavelength of black body radiation defined as:

$$\lambda_p(T_{eff}) = \frac{b}{T_{eff}}, \quad (21)$$

where $b \approx 2.898 \times 10^{-3}$ m K is Wien's displacement constant.

The Pseudo-Huber-loss function in Eq. (19) is used, as it is robust to outliers. This is needed, as there is some uncertainty about the star spectra, which can possibly lead us to use inaccurate target DN counts for some stars. Residuals higher than 6 begin to affect the optimization cost only linearly instead of quadratically. The transition from the quadratic to the linear regime is smooth, i.e., the derivatives are continuous for all degrees. This outlier limit will be determined heuristically during calibration.

2.4. The Moon (c^{moon})

At 19:20 UTC on December 14, 2018, the Suomi 100 satellite captured an image of a waxing Moon almost at first quarter (see Figure 10). The image also has a slice of Earth, quite saturated. Luckily, upon closer inspection, it can be noted that only the red channel is saturated for the Moon.

Our calibration measurement is the DNs induced by moonlight. It is completed in much the same way as for the stars. First, the image-processing chain is inverted to get an estimate of the raw, unprocessed image. The background pixel activation is estimated by selecting an empty patch of space in the image and calculating the average pixel value there. Background subtracted pixel values are then summed from a half-circle-shaped mask placed on top of the Moon for the final measure (see Table 5).

We also need the predicted DN counts, which can be calculated by integrating Eq. (4) over the wavelength, provided that we have the full-disk integrated spectral irradiance of the Moon at the time the image was taken. For this, we use the ROLO Lunar reflectance model (Kieffer and Stone, 2005) together with the moon phase information from mainly NASA (NASA, 2018) (see Table 6), and the solar spectral irradiance data for the imaging date from the NOAA Climate Data Record (Coddington et al., 2019).

The ROLO model gives the disk-equivalent albedo (λ_l) for 32 different bands l that cover a wavelength range of 330-2420 nm. Each band is associated with an effective wavelength (λ_l). The model is defined as:



Figure 10: Image #748 of the first quarter Moon. The image was taken with $T = 2.4$ ms exposure and a total gain of $G = 1$. Left: On-board processed image. Right: Closeup of the Moon seen on the left image.

Table 5: Moonlight-Induced Digital Numbers (DNs) in the Analyzed Moon Image

Channel	DNs
Red \hat{Q}_R^{moon}	111,090 ^a
Green \hat{Q}_G^{moon}	101,935
Blue \hat{Q}_B^{moon}	86,252

^a with saturated pixels

Table 6: Observational Details of the Moon at the Time of the Analyzed Moon Image

Date and time	2018-12-14 19:20 UTC
Earth-Moon distance d	402,088 km (NASA, 2018)
Sun-Earth distance D	0.98446 AU (USGS, 2019)
Sub-Earth latitude θ , longitude ϕ	5.000°, -4.246° (NASA, 2018)
Sub-solar latitude Θ , longitude Φ	0.932°, 93.416° (NASA, 2018)
Phase angle g	97.55° ^a
Moon solid angle @ 384,400 km	6.4177×10^{-5} sr (Keiffer and Stone, 2005)
Moon solid angle Ω^{moon} @ d	5.863×10^{-5} sr ^b

^a Calculated from Sub-Earth and Sub Solar coordinates^b Solid angle is inversely proportional to the distance squared

$$\ln A_l = \sum_{i=0}^3 a_{i,l} g^i + \sum_{j=1}^3 b_{j,l} \Phi^{2j-1} + c_1 \theta + c_2 \phi + c_3 \Phi \theta + c_4 \Phi \phi + d_{1,l} e^{-g/p_1} + d_{2,l} e^{-g/p_2} + d_{3,l} \cos[(g - p_3)/p_4],$$

where the model parameters $a_{(\cdot),l}$, $b_{(\cdot),l}$, $c_{(\cdot)}$, $d_{(\cdot),l}$, and $p_{(\cdot)}$ are all given in the source article (Kieffer and Stone, 2005). The predictors for the effective disk albedo (A_l) are the phase angle (g), the selenographic latitude (θ) and longitude (ϕ) of the observer, and finally, the selenographic longitude of the Sun (Φ). The model is stated to be valid for phase angles between 90°, which puts the $g = 97.55^\circ$ out of that range. However, the values of the model parameters were estimated based on the imaging data with phase angles up to 97°, which gives us some confidence that the model will still yield a useful reference for our use case.

The irradiance of the Moon (I_l^{moon}) at a given band l is given by Kieffer and Stone (2005) as:

$$I_l^{moon} = A_l \Omega^{moon} I_l^{sun} / \pi, \quad (23)$$

where Ω^{moon} is the solid angle of the Moon and I_l^{sun} is the irradiance of the Sun at band l .

For our purposes of numerical integration with the camera quantum efficiency function, we will use linear interpolation for the effective disk albedos. This gives us the following expression to integrate with our camera model (Eqs. (3), (4), and (6)) for the predicted full disk DN responses:

$$Q_k^{moon} = u_{max} G W^{-1} T A \frac{\Omega^{moon}}{\pi}. \quad (24)$$

$$\int_{\lambda_{min}}^{\lambda_{max}} h_k(\lambda) E_\gamma(\lambda)^{-1} A(\lambda) I^{sun}(\lambda) d\lambda,$$

where the wavelength-dependent albedo $A(\lambda)$ is linearly interpolated based on the 32 effective wavelengths λ_l and the corresponding albedos A_l . In addition, the solar spectral irradiance $I^{sun}(\lambda)$ is linearly interpolated from the table given by Coddington et al. (2019) and adjusted to the correct distance by scaling with $(1 \text{ AU} / D)^2$. The interpolated function values are shown in Figure 11.

Finally, the Moon measurements contribute the following Moon cost terms (c_k^{moon}) for the least-squares method:

$$c_k^{moon} = (\log Q_k^{moon} - \log \hat{Q}_k^{moon})^2, k \in \{G, B\} \quad (25)$$

where the measurement for the saturated R channel was discarded.

2.5. The prior (c^{moon}) and the full cost vector (c)

In addition to the cost terms derived from the measurements extracted from images taken in the laboratory, the star image and the moon image, we use a prior over the quantum efficiency function parameters, which corresponds to the following cost term vector:

$$c_k^{prior} = w_p^2 (h_{0,k} - h_{0,k}^{prior})^2, \quad (26)$$

where w_p is a prior weight term, $h_{0,k}$ are the current estimates for the parameters, and $h_{0,k}^{prior}$ are the prior values for them, defined based on the curves from the

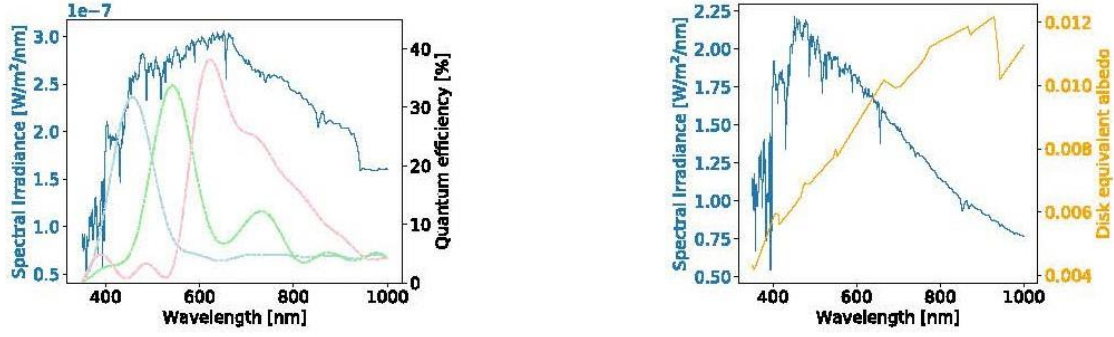


Figure 11: Left: The Moonlight spectral irradiance on December 14, 2018 (the blue solid line). It is derived from the ROLO-model effective disk albedo (right side figure, the orange line) and the Sun's spectral irradiance (right figure, the blue line). The left figure shows also the initial joint sensor-optics quantum efficiency curves, based on their respective datasheet values (red, green and blue dashed lines), and modeled by our interpolation function in Eq. (6).

datasheets (refer to Figure 3). The full cost vector is thus:

$$\mathbf{c} = \begin{bmatrix} \mathbf{c}_{8 \times 1}^{lab} \\ \mathbf{c}_{3M \times 1}^{stars} \\ \mathbf{c}_{2 \times 1}^{moon} \\ \mathbf{c}_{3N_c \times 1}^{prior} \end{bmatrix} \quad (27)$$

where the subscripts indicate the sizes of the different vectors given by equations (12), (18), (25), and (26); $M = 10$ is the number of matched stars; and $N_c = 14$ is the number of control parameters for the quantum efficiency function of one of the RGB channels. All cost terms have equal weights, except those related to the stars, which are discounted by a weight term $w_m \in [0,1]$ that is calculated based on the stars' effective temperatures using Eq. (20).

2.6. The calibrated quantum efficiency functions

In total, we have 82 equations and 43 free parameters in Eq. (27) to optimize the quantum efficiency functions. We experimented with different values for the measurement outlier limit and the prior weight before settling on $\delta = 0.2$ and $w_p = 0.2$, respectively. The resulting quantum efficiency curves are shown in Figure 12, and the predicted and measured DN counts for stars and the Moon are shown in Figure 13 and in Table 7. Overall, the average deviation between predictions and measurements changes from 14.7% to 7.50% during calibration.

The resulting predicted ratios for the laboratory measurements are $\beta_{rg} = 0.267$ and $\beta_{bg} = 0.227$, of which the second one corresponds well to the measurements, which were $\bar{\beta}_{bg} = [0.23, 0.24, 0.21, 0.22]^T$. The first ratio is a slightly different from the measurements $\bar{\beta}_{rg} = [0.26, 0.25, 0.24, 0.24]^T$. This might be because the quantum efficiency functions of both red and green channels change greatly in opposite directions at $\lambda_{gr} = 557.7$ nm, and the limited spectral resolution of the model does not allow to accurately model a narrow band in this region.

The Moon measurements are closely matched by the predicted DNs for the non-saturated green and blue channels. The predicted red channel DN count seems reasonable, as the measurement was only slightly saturated.

Based on the star measurements, the PSF standard deviation was estimated as $\sigma = 1.877$ px. The star measurements are quite noisy due to the high gain settings used when taking the image (see Figure 9), which leads to many of the stars having a discrepancy of more than 10% with at least one channel. Three stars (Bellatrix, Alnilam, and Alnitak) are all modeled as dimmer than what the measurements suggest. These stars are listed as variable stars in the General Catalog of Variable Stars (Samus' et al., 2017). Based on the limits of variability given in the catalog and the visual magnitudes used during calibration, the variability could explain around 55%, 35%, and 20% of the discrepancy, respectively. At the time of writing only one of the star images was downlinked. If we had had more

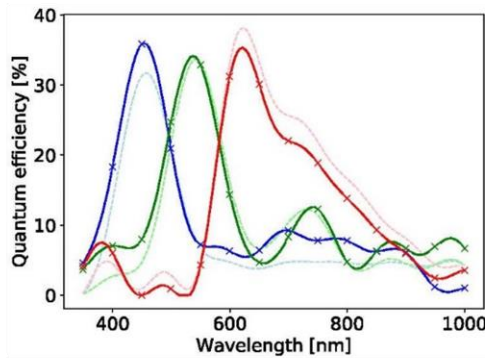


Figure 12: Quantum efficiency functions after calibration. The control points are shown with crosses and the prior quantum efficiency functions are shown with dashed, light-colored lines.

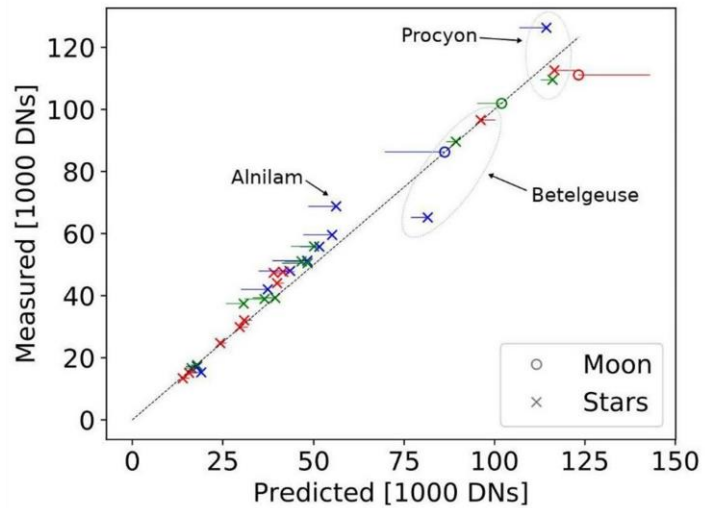


Figure 13: The resulting predicted DN counts for each channel for the ten non-excluded stars listed in Table 4, and one set of DN counts from the Moon image (see Table 5) versus the measured ones. The red, blue and green colors correspond to R-, G-, and B-channels, respectively. The lines show how the predicted DNs change as a result of calibration, specifically, the free line endings correspond to predictions using the initial quantum efficiency functions.

images, we could have better estimated the measurement noise from multiple images.

It is conceivable that the undetermined saturation at $u_{max} = 567$ stems from the same root cause as the lab-observed slight non-linearity of the sensor response. However, we can only speculate what this root cause might be. The non-linearity could also be related to the automatic dark-level subtraction performed by the image sensor. However, after some investigation, this seems unlikely as the dark-image background activation levels match closely with the background levels of the corresponding actual images. Another explanation could be that the on-board image-processing software implements the gamma correction slightly differently than how we think. For example, if we use a gamma break parameter value of 0.09 instead of 0.10, the non-linearity disappears.

As the non-linearity was not taken into account explicitly, the estimated PSF standard deviation σ might partially compensate for it in relation to the saturating star measurements. This would result in a smaller σ than what it actually is. This would also make the model over-estimate the Moon measurement

Table 7: Comparison between the Predicted (Pred.) and Measured (Meas.) RGB Values of the Analyzed Stars

Name	Red			Green			Blue		
	Meas.	Pred.	$\Delta\%$	Meas.	Pred.	$\Delta\%$	Meas.	Pred.	$\Delta\%$
Procyon	113	117	3.5	110	116	5.9	126	114	-9.5
Betelgeuse	96.6	96.2	-0.4	89.6	89.3	-0.3	65.2	81.5	25
Bellatrix	44.0	40.0	-9.1	51.1	46.7	-8.6	55.7	51.6	-7.5
Alnilam	47.7	41.7	-13	55.9	50.1	-10	68.8	56.2	-18
Alnitak	47.4	39.1	-17	50.5	48.3	-4.3	59.6	55.1	-7.5
Mirzam	32.1	30.9	-3.5	39.3	39.5	0.6	51.2	48.2	-5.9
Saiph	29.9	29.7	-0.5	38.9	36.6	-6.1	48.0	43.5	-9.4
Mintaka	24.7	24.3	-1.5	37.4	30.8	-18	42.0	37.5	-11
Cursa	15.1	15.7	3.9	17.7	17.9	1.6	15.3	19.1	25
Gomeisa	13.4	14	4.2	16.7	16.4	-1.8	17.2	17.9	4.2
Moon	111 ^a	123	11	102	102	0.0	86.3	86.2	0.0

Note that light and dark gray cells indicate a discrepancy of more than 10% and 15%, respectively.

^a Red channel for the Moon was ignored, as it was saturated.

DNs, which would introduce a negative bias for the calibrated B- and G-channel quantum efficiency functions (the Moon measurement of the R-channel was ignored). However, such a bias is not obvious when examining Figure 12.

Overall, considering the limited measurements available, we are content with the calibration results. We summarize the main lessons learned about the calibration of a satellite's camera payload in the Section 4.

3. Aurora

On January 22, 2019 at 18:08:20 UTC, one day before the star image was captured, the satellite captured an image of a faint, but unmistakable aurora borealis (see Figures 14 and 15).



Figure 14: On-board processed image #1229 of an aurora. The image was taken with $T = 2.4$ s exposure and a total gain of $G = 128$.

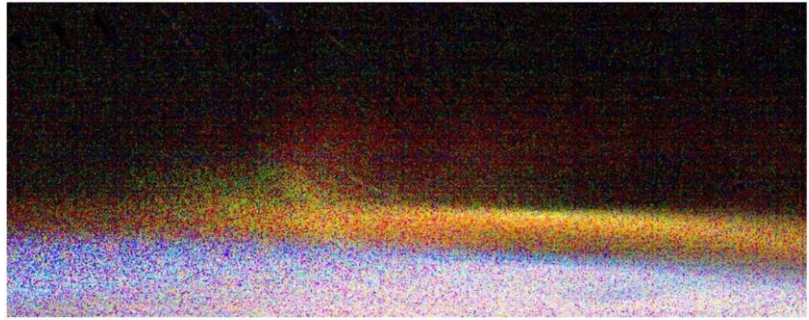


Figure 15: A closeup of the aurora as seen in Figure 14 after warm pixel compensation and an adjustment to the image brightness.

The star image (Figure 6) is used to remove the effect of warm pixels. There is some motion blur present, and it is easy to see from the stars and city lights that the pole of the satellite rotation axis is at the bottom left part of the image. In the middle of the image, just above the yellow glowing sodium airglow layer, the aurora is glowing red at high altitudes and green at lower altitudes. The sodium layer emitting at wavelengths of 589.0 nm and 589.6 nm is typically 5 km thick and between the altitudes of 80–105 km. Blue and green auroral emissions at 427.8 nm and 557.7 nm, respectively, usually occur at altitudes between 90–130 km, while the red emissions at 630 nm are predominantly produced at altitudes higher than 200 km (Nozawa et al., 2018).

Based on our calibrated camera model and the aurora image, our goal is to roughly estimate the luminosity of the imaged aurora at different emission lines. Without additional constraints, we can only estimate luminosities at three different emission lines at a time,

as we only have three measurement channels (R, G, and B).

We proceed by defining five rectangles in the image (see Figure 16), avoiding regions in the image with negative spots produced by the stars that are present in the image used for warm pixel compensation. The first rectangle is selected so that it corresponds to emissions mainly at 630 nm (red) and the motion blur affects it the least (region index $r = 1$). The second rectangle ($r = 2$) was placed on an image region that seemed to have the strongest emissions at 630 nm, while also having some emissions at 557.7 nm (green). The third

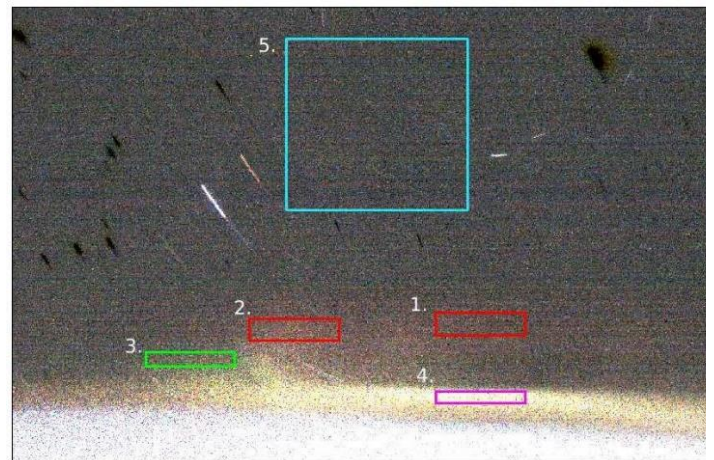


Figure 16: Different regions as seen in Figure 15 defined by rectangles. Extra $\times 2$ gain, and a background level was added so that the negative spots are visible

rectangle ($r = 3$) was placed where the 557.7 nm emissions are the strongest. The fourth rectangle ($r = 4$) was placed where the sodium layer seems the strongest due to the motion blur being in the same direction as the

layer itself. Finally, the fifth rectangle ($r = 5$) used for background subtraction is placed at an empty region of the image with no emissions or disturbances from the negative star image.

We calculate the mean pixel response $\hat{q}_{r,k}$ of each channel k at each rectangle r and then subtract the mean pixel response of the background rectangle from the mean pixel response of the other rectangles. We approximate the pixel solid angles with the solid angle Ω_r of the central pixel of each rectangle. The central pixel solid angles are calculated using Eq. (2). By grouping the two sodium lines into a single line at 589.3 nm, we model all the emissions using three of the four emission lines. For unit radiance at each emission line, we can calculate the predicted DN_s recorded at each RGB channel by using the camera model equations (3), (4), and (6):

$$q_{r,l,k} = u_{max} G W^{-1} T A \Omega_r h_k(\lambda_l) E_\gamma(\lambda_l)^{-1}, \quad (28)$$

where λ_l is the wavelength of the emission line l . For each region, using the pseudo-inverse method, we can solve the emission line radiances by:

$$\begin{aligned} \hat{q}_r &= Q_r r_r \\ \Rightarrow r_r &= (Q_r^T Q_r)^{-1} Q_r^T \hat{q}_r, \end{aligned} \quad (29)$$

where Q_r is a matrix composed using Eq. (28) with rows corresponding to channels and columns to emission lines, \hat{q}_r is a vector with mean channel responses, and r_r is a vector with estimated radiances for each emission line of a region r . As only three emission lines can be estimated for one region, the 589.3 nm sodium line is only used for the sodium region, where it substitutes the 630.0 nm emission line. Our estimates are based on the assumption that all emissions occur at the three selected wavelengths. In literature, the luminosity of aurorae is usually given in kilo-Rayleigh (kR) instead of $W/m^2/sr$. Rayleigh is a unit of photon flux I , and it can be calculated from radiance R using $I = 4\pi \cdot 10^{-10} E_\gamma(\lambda)^{-1} R$. Mean responses and resulting photon fluxes are presented in Table 8.

It is informative to compare the simulated auroral emission intensities with the auroral emission intensities observed from the ground. Emission intensities

depend on geomagnetic conditions but the emission at 557.7 nm (green) has been estimated to be about 1 kR during geomagnetically-quiet conditions and about 10 kR during geomagnetically-active nightside conditions (Michell, 2020). The emission at 427.8 nm (blue) has, instead, been estimated to be 100–500 R (Shikawa et al., 2019). Statistical estimation of the dayside (06–18 MLT) auroral emission has, in turn, provided emission rate at 630 nm to be 0.2–3.9 kR, and the green (557.7 nm) 0.1–17.3 kR (Qi et al., 2017). Although one cannot make a detailed comparison between a single observation made in space and statistical observations based on ground-based observations, the derived auroral emissions shown in Table 8 are in the magnitude range where auroral emission intensity is expected to be.

4. Discussion

Calibration of a camera instrument that is launched to space is of fundamental importance for the accurate usage of the obtained images. However, even if the camera is well calibrated on ground, the obtained calibration values do not necessarily describe the camera instrument that has waited a long time before the launch, and whose properties may have changed during the launch (see e.g., Bertaux et al. (2006); Figure 11). Moreover, properties of camera sensors change over time, and therefore, a continuous in-space calibration is needed.

The calibration issue can be especially severe for cameras on small satellites because these projects (which are, for instance, university-based and student-

Table 8. Aurora Photon Fluxes

r	Patch	Red [DN]	Green [DN]	Blue [DN]	427.8 [kR]	557.7 [kR]	589.3 [kR]	630.0 [kR]
1	Clean Red	29.2	12.3	6.7	0.0898	0.827		2.87
2	Strong Red	61.3	31.4	22.3	1.07	2.18		5.77
3	Green	50.5	43.8	26.6	1.51	3.97		4.44
4	Sodium	315.7	254.0	164.5	9.69	2.11	42.7	

The columns from the left to right are: The index (r) of the analyzed position in the analyzed aurora image (see Figure 16), characteristic features of the regions r , counts in red, blue and green channels in the region r , and the derived emission intensity in kR.

driven) can have very limited budgets that make it almost impossible to perform a comprehensive calibration campaign. The storage and transportation of a small satellite and its payload can also prove to be risky and result in instrument contamination and mechanical malfunctions. A camera for a small satellite can often be bought off-the-shelf and is not made in-house. Therefore, all critical information about the camera and its image-processing algorithms may not be available.

In this work, we tried to overcome the problems that occurred when images of the Suomi 100 CubeSat were analyzed. The analysis of the images was complicated, especially because of the limited on-ground calibration, on-board image compression (jpg) due to the limited telemetry rate, and the satellite's rotation, which reduced the maximum exposure time.

The performed calibration is based on minimizing a cost function using least-squares fitting. Measurement noise models were not used to weigh different measurements. This was a conscious decision stemming from the large uncertainties; we had about the unknown errors of the source models. For example, many of the stars imaged have variable brightness, and possibly even variable spectra. It seemed too difficult to formulate a noise model that would have taken these uncertainties into account. A simplified noise model would have severely underestimated the errors and possibly would have led to nonsensical results.

During the study, we tried the calibration based only on the star measurements and then verifying the result, using the Moon and laboratory measurements. However, this resulted in the Moon B-channel prediction being too low by 23%, while the Betelgeuse B-channel measurement being matched accurately. When including all the measurements, the Moon B-channel is matched accurately, while the Betelgeuse B-channel prediction is 25% too high. If we exclude both the Moon and the Betelgeuse measurements from the calibration, the Moon B-channel prediction is 13% too low and the Betelgeuse prediction 17% too high. The other predictions were relatively stable across these variations. As the Betelgeuse low B-channel measurement could possibly be explained by the dimming event, we opted to use all the measurements dur-

ing calibration. If any future analysis of the aurora image would be conducted, it might be possible to establish somewhat reasonable error bars on the emission line radiances by performing the calibration and subsequent radiance estimation multiple times in a leave-one-out scheme, where each measurement is excluded in turn.

The main lessons learned from our investigations can be summarized as:

- Avoid unnecessary on-board preprocessing of measurements, particularly the kind that cannot be reversed.
- Make certain you have a calibrated model for your sensor before sending it to space.
- The Moon is a good calibration target, provided that more than half of it is illuminated.
- Stars can be used for calibration, provided that it is possible to obtain reliable reference spectra and multiple images of the same star field with different exposures and only limited motion blur.

Thus, we would recommend that during small satellite development a camera model is defined, its parameters determined, and its correctness verified based on laboratory measurements probing different aspects of the model:

- *Response curve, dark current, structured noise, readout noise:*
 - Image a light source of constant intensity with varying exposure time, from as short as possible until saturation. Change light source brightness and repeat. Include a batch with the lens cap installed.
 - Same as above but vary gain setting instead of exposure time. Lens cap images can be skipped.
- *Point spread function:* Image a high-resolution computer screen with different calibration patterns; see, for instance, Mosleh et al. (2015).
- *Glare:* Image a dark area while gradually turning the camera towards a bright light source, possibly the Sun; see, for example, Martin (1972).
- *Geometric distortions:* 30–50 images of a chessboard pattern in different poses; see, for

instance, OpenCV documentation (OpenCV, 2022).

All the above measurements can be performed without a monochromator. Raw images should be obtained and multiple ones (three to five) should be taken with each configuration. If some on-board processing is to be done, it should be modeled and validated separately. If a monochromator can be used, then the quantum efficiency function could be determined by taking measurements with as many equally spaced wavelengths as is feasible. A perfect setup for our use case would allow us to take measurements at the significant atmospheric line emission wavelengths (at least at 427.8 nm, 557.7 nm, 589.3 nm, and 630.0 nm) using a FWHM of 1 nm and then determine the overall shape of the quantum efficiency function by measuring the wavelength range 350–1000 nm using a 10 nm spacing and a FWHM of 10 nm.

The main approach introduced in this article was to use existing real space objects, the Moon and stars, as space-based calibration sources. The analysis demonstrated that when models of the intensity and spectral shape for these objects are developed, a comparison between the simulated RGB values and the observed RGB values enables space-based calibration. Most importantly, such a calibration can be made continuously during the whole lifetime of the camera instrument and in such a way as to reduce the problems caused by degradation of the camera sensors. It can be foreseen that the developed calibration method can increase the usage of the images from small satellites and, therefore, motivate the inclusion of additional camera instruments on small satellites.

5. CONCLUSIONS

We have investigated how to optimize the use of a camera instrument on a small satellite. We have developed image-processing and camera calibration methods, and demonstrated the applicability of the methods by using images taken by the Suomi 100 satellite. The analysis shows how the problems caused by the limited on-ground calibration and other common small satellite limitations can be partly overcome by using images of the Moon and stars, and to provide continuous camera calibration in space. As an example of the

applicability of the developed methods, we have estimated the auroral emission intensities from the image taken by the satellite. The analysis implies that the developed camera calibration methods can be used to maximize the reliability and applicability of camera instruments on small satellites.

Acknowledgements

The authors would like to thank the Academy of Finland (Project Nro 310444), Magnus Ehmrooth foundation, and the Finnish Prime Minister's Office for the financial support of the Suomi 100 satellite project. EK thanks Jari Mäkinen for the Suomi 100 satellite outreach activities.

References

-
- Aptina Imaging Corporation (2006): Aptina MT9T031 Datasheet. Available at: <https://uk.rs-online.com/webdocs/0d2f/0900766b80d2f066.pdf> (accessed Aug. 18, 2020).
 - Bertaux, J. L., Korabiev, O., Perrier, S., Quémerais, E., Montmessin, F., Leblanc, F., Lebonnois, S., Rannou, P., Lefèvre, F., Forget, F., Fedorova, A., Dimarellis, E., Reberac, A., Fonteyn, D., Chaufray, J. Y., and Guibert, S. (2006): SPI-CAM on Mars Express: Observing Modes and Overview of UV Spectrometer Data and Scientific Results, *J. of Geophysical Research: Planets*, Vol. 111(E10). doi: 10.1029/2006JE002690.
 - Bertaux, J. L., Kyrölä, E., Fussen, D., Hauchecome, A., Dalaudier, F., Sofieva, V., Tamminen, J., Vanhellemont, F., Fanton d'Andon, O., Barrot, G., Mangin, A., Blanot, L., Lebrun, J. C., Pérot, K., Fehr, T., Saavedra, L., Leppelmeier, G. W., and Fraisse, R. (2010): Global Ozone Monitoring by Occultation of Stars: An Overview of GOMOS Measurements on ENVISAT, *Atmospheric Chemistry and Physics*, Vol. 10(24), pp. 12,091–12,148. doi: 10.5194/acp-10-12091-2010.
 - Castelli, F. and Kurucz, R. L. (2004): New Grids of ATLAS9 Model Atmospheres, *arXiv preprint astro-ph/0405087*.

- Coddington, O., Lean, J. L., Lindholm, D., Pilewskie, P., and Snow, M. (2019): NOAA Climate Data Record (CDR) of Solar Spectral Irradiance (SSI), NRLSSI Version 2. Available at: <https://www.ncei.noaa.gov/thredds/catalog/cdr-spectral-solar-irradiance/daily/catalog.html> (accessed Oct. 14, 2020).
- Díaz-Francés, E. and Rubio, F. J. (2013): On the Existence of a Normal Approximation to the Distribution of the Ratio of Two Independent Normal Random Variables, *Statistical Papers*, Vol. 54(2), pp. 309–323. doi: 10.1007/s00362-012-0429-2.
- Jos. Schneider Optische Werke GmbH (2008): Cinegon 1.4/8 Datasheet. Available at: <https://schneiderkreuznach.com/application/files/2315/0781/8893/optical-data-sheet-cinegon.pdf> (accessed Aug. 18, 2020).
- Kafka, S. (2020): AAVSO International Database. Available at: <https://www.aavso.org>.
- Kieffer, H. and Stone, T. C. (2005): The Spectral Irradiance of the Moon, *The Astronomical J.*, Vol. 129, pp. 2887–2901. doi: 10.1086/430185.
- Laidler, V. G., Greenfield, P., Busko, I., and Jedrzejewski, R. (2008): Pysynphot: A Python Re-Implementation of a Legacy App in Astronomy, in *Proc. of the 7th Python in Science Conf.*, pp. 36–38. Available at: https://hal.archives-ouvertes.fr/hal-00502586/file/SciPy2008_proceedings.pdf#page=39.
- Luo, W., Huang, J., and Qiu, G. (2010): JPEG Error Analysis and Its Applications to Digital Image Forensics, *IEEE Trans. on Information Forensics and Security*, Vol. 5(3), pp. 480–491. doi: 10.1109/TIFS.2010.2051426.
- Martin, S. (1972): Glare Characteristics of Lenses and Optical Instruments in Visible Region, *Optica Acta*, Vol. 19 (6), p. 499. doi: 10.1080/713818610.
- MathWorks (2006): Gamma Correction. Available at: <https://se.mathworks.com/help/vision/ref/gamma-correction.html> (accessed Aug. 18, 2020).
- Mazonka, O. (2012): Solid Angle of Conical Surfaces, Polyhedral Cones, and Intersecting Spherical Caps, *arXiv preprint arXiv: 1205.1396*. doi: 10.48550/arXiv.1205.1396.
- McDonald, I., Zijlstra, A. A., and Watson, R. A. (2017): Fundamental Parameters and Infrared Excesses of Tycho-Gaia Stars, *Monthly Notices of the Royal Astronomical Soc.*, Vol. 471(1), pp. 770–791. doi: 10.1093/mnras/stx1433.
- Michell, R. G. (2020): Auroral Structure and Dynamics from GOLD, *J. of Geophysical Research: Space Physics*, Vol. 125(3), p. e2019JA027,650. doi: 10.1029/2019JA027650.
- Mosleh, A., Green, P., Onzon, E., Begin, I., and Pierre Langlois, J. (2015): Camera Intrinsic Blur Kernel Estimation: A Reliable Framework, in *Proc. of the IEEE Conf. on Computer Vision and Pattern Recognition*, pp. 4961–4968. doi: 10.1109/CVPR.2015.7299130.
- NASA (2018): Moon Phase and Libration, 2018. Available at: https://svs.gsfc.nasa.gov/vis/a000000/a004600/a004604/mooninfo_2018.txt (accessed Aug. 18, 2020).
- Nozawa, S., Kawabata, T., Hosokawa, K., Ogawa, Y., Tsuda, T., Mizuno, A., Fujii, R., and Hall, C. (2018): A New Five-Wavelength Photometer Operated in Tromsø (69.6° N, 19.2° E), *Earth, Planets and Space*, Vol. 70(1), p. 193. doi: 10.1186/s40623-018-0962-x.
- Ochsenbein, F., Bauer, P., and Marcout, J. (2000): The VizieR Database of Astronomical Catalogues, *Astronomy and Astrophysics Supplement Series*, Vol. 143 (1), pp. 23–32. doi: 10.1051/aas:2000169.
- OpenCV (2022): OpenCV: Camera Calibration. Available at: https://docs.opencv.org/4.x/de/dbb/tutorial_py_calibration.html (accessed Apr. 8, 2022).
- Perryman, M. A. C., Lindegren, L., Kovalevsky, J., Hog, E., Bastian, U., Bernacca, P. L., Creze, M., Donati, F., Grenon, M., Grewing, M., van Leeuwen, F., van der Marel, H., Mignard, F., Murray, C. A., Le Poole, R.S., Schrijver, H., Turon, C., Arenou, F., Froeschle, M., and Petersen, C. S. (1997): The HIPPARCOS and TYCHO Catalogues. Astrometric and Photometric Star Catalogues Derived from the ESA HIPPARCOS Space Astrometry Mission, in *ESA Special Publication*, Vol. 1200 of ESA Special Publication. Available at: <https://ui.adsabs.harvard.edu/abs/1997A&A...323L..49P>.

- Qi, Q., Hui-Gen, Y., Quan-Ming, L., and Ze-Jun, H. (2017): Correlation Between Emission Intensities in Dayside Auroral Arcs and Precipitating Electron Spectra, *Chinese J. of Geophysics*, Vol. 60 (1), pp. 1 - 11. doi: 10.1002/cjg2.30023.
- Ramírez, S. V., Sellgren, K., Carr, J. S., Balachandran, S. C., Blum, R., Terndrup, D. M., and Steed, A. (2000): Stellar Iron Abundances at the Galactic Center, *The Astrophysical J.*, Vol. 537(1), p. 205. doi: 10.1086/309022.
- Samus', N. N., Kazarovets, E. V., Durlevich, O. V., Kireeva, N. N., and Pastukhova, E. N. (2017): General Catalogue of Variable Stars: Version GCVS 5.1, *Astronomy Repts.*, Vol. 61(1), pp. 80 - 88. doi: 10.1134/S1063772917010085.
- Shiokawa, K., Otsuka, Y., and Connors, M. (2019): Statistical Study of Auroral/Resonant-Scattering 427.8-Nm Emission Observed at Subauroral Latitudes Over 14 Years, *J. of Geophysical Research: Space Physics*, Vol. 124(11), pp. 9293 - 9301. doi: 10.1029/2019JA026704.
- Soubiran, C., Le Campion, J. F., Brouillet, N., and Chemin, L. (2016): The PASTEL Catalogue: 2016 Version, *Astronomy & Astrophysics*, Vol. 591, p. A1118. doi: 10.1051/0004-6361/201628497.
- Stetson, PB. (1987): DAOPHOT: A Computer Program for Crowded-Field Stellar Photometry, *Publications of the Astronomical Soc. of the Pacific*, Vol. 99(613), p. 191. doi: 10.1086/131977.
- Tamminen, J., Kyrölä, E., Sofieva, V. F., Laine, M., Bertaux, J. L., Hauchecorne, A., Dalaudier, F., Fussen, D., Vanhellemont, F., Fanton-d'Andon, O., Barrot, G., Mangin, A., Guirlet, M., Blanot, L., Fehr, T., de Miguel, L. S., and Fraisse, R. (2010): GOMOS Data Characterisation and Error Estimation, *Atmospheric Chemistry and Physics*, Vol. 10 (19), pp. 9505–9519. doi: 10.5194/acp-10-9505-2010.
- USGS (2019): Earth-Sun Distance in Astronomical Units for Days of the Year. Available at: <https://www.usgs.gov/media/files/earth-sun-distance-astronomical-units-days-year> (accessed Oct. 14, 2020).
- Wenger, M., Ochsenbein, F., Egret, D., Dubois, P., Bonnarel, F., Borde, S., Genova, F., Jasiewicz, G., Laloë, S., Lesteven, S., and Monier, R. (2000): The SIMBAD Astronomical Database - The CDS Reference Database for Astronomical Objects, *Astronomy and Astrophysics Supplement Series*, Vol. 143 (1), pp. 9–22. doi: 10.1051/aas:2000332.
- Whittaker, E.T. (1915): XVIII. On the Functions Which are Represented by the Expansions of the Interpolation Theory, *Proc. of the Royal Society of Edinburgh*, Vol. 35, pp. 181–194. doi: 10.1017/S0370164600017806.
- Wu, Y., Singh, H. P., Prugniel, P., Gupta, R., and Koleva, M. (2011): Coudée-Feed Stellar Spectral Library - Atmospheric Parameters, *Astronomy & Astrophysics*, Vol. 525, A71. doi: 10.1051/0004-6361/201015014.